Loading-induced stress variation on active faults and seismicity modulation in the Kuril Islands-Japan region

Earth Planet. Sci. Lett. 643 (2024) 118904

Contents lists available at ScienceDirect

Earth and Planetary Science Letters

journal homepage: www.elsevier.com/locate/epsl

Loading-induced stress variation on active faults and seismicity modulation in the Kuril Islands-Japan region

Yiting Cai *, Maxime Mouyen

Department of Space, Earth, and Environment, Chalmers University of Technology, Gothenburg, 41296, Sweden

ARTICLE INFO

Editor: J.P. Avouac

Keywords:
Coulomb stress change
Seismicity
Surface loads
Subduction zone

ABSTRACT

The Earth's crust experiences continual stress variations due to the loads of the ocean, atmosphere, and continental water. We investigate if these stress variations can influence the seismicity of the Kuril megathrust, a part of the subduction zone positioned between the Pacific and Okhotsk plates, in the Kuril Islands-Japan region. Using established fault geometries and loading-induced stress variations, we calculate monthly Coulomb stress change resulting from hydrological, atmospheric, and non-tidal ocean loads, as well as their combined effects, from 2005 to 2016. We subsequently compare these stress variations with the observed monthly seismic rate along the Kuril megathrust during the same period. Our analysis reveals a weak but statistically significant positive correlation between the multi-loading-induced Coulomb stress changes and seismic activity, particularly in the shallow segment of the southern Kuril trench near Hokkaido island. This finding suggests that relatively small Coulomb stress changes, on the order of a few kPa, induced by surface loads, have the potential to locally trigger earthquakes within stressed fault systems. We also show that the summed contribution of atmospheric, non-tidal oceanic, and hydrological loads to this seismic triggering differs from the results obtained when taking each load separately. In addition, the relative contribution of each load to the Coulomb stress change varies as a function of time and space. Anticipating future studies, we emphasize the importance of extending the research throughout the entire study period and the interest in considering the cumulative impact of multiple loading sources when investigating their role in seismic activity.

1. Introduction

The possible influence of non-tectonic forces in earthquakes' triggering has long been studied, focusing first on tidal forces (e.g. Tsuruoka et al., 1995; Tanaka et al., 2004; Scholz et al., 2019; Yan et al., 2023) and then extending to a vast amount of surface loads, such as continental water (Bettinelli et al., 2008; Craig et al., 2017; Johnson et al., 2020; Hsu et al., 2021; Xue et al., 2021), air pressure (Gao et al., 2000), sea-level (Luttrell and Sandwell, 2010; Lordi et al., 2022) or erosion (Steer et al., 2020).

Indeed, all these processes involve the redistribution of a large amount of mass at the earth's surface, which in turn deforms and changes the state of stress in the crust and on the fault planes that lie in. However, it is worth noting that one could expect a combined influence of the processes mentioned above since they can take place within the same spatial and temporal window. Thus, a way to clarify their influence on earthquake triggering is to study their cumulative effect (Lowry, 2006), rather than focusing on one particular process. Following this idea, we examine the influence of stress variations due to the cumulative effect of three surface loads, namely non-tidal ocean, atmosphere, and hydrology, on the earthquake occurrence in the subduction zone of the Kamchatka-Kuril Islands-Japan region between 2005 and 2016. Seasonal variations in seismicity have long been suspected in the area and several recent studies have found the stress variations induced by the hydrological loadings (snow and rainfalls) can influence the seasonal occurrence of seismicity (Heki, 2003; Ueda and Kato, 2019; Ueda et al., 2024). To investigate the loading-induced seismicity and find the areas that are sensitive to non-tectonic processes in the Kamchatka-Kuril Islands-Japan region, our approach is to compute Coulomb stress change induced by the cumulative effects of hydrological, atmospheric, and non-tidal ocean loadings on the Kuril megathrust, from 2005 to 2016 and to evaluate if they correlate with the variations of seismicity in the area.

We first introduce the various datasets needed for our study, specifically, the stress variations due to the hydrological, atmospheric, and non-tidal ocean loadings, the geometry model of the Kuril megathrust,

* Corresponding author.
E-mail addresses: yiting.cai@chalmers.se (Y. Cai), maxime.mouyen@chalmers.se (M. Mouyen).

https://doi.org/10.1016/j.epsl.2024.118904
Received 10 April 2023; Received in revised form 29 May 2024; Accepted 19 July 2024
Available online 26 July 2024

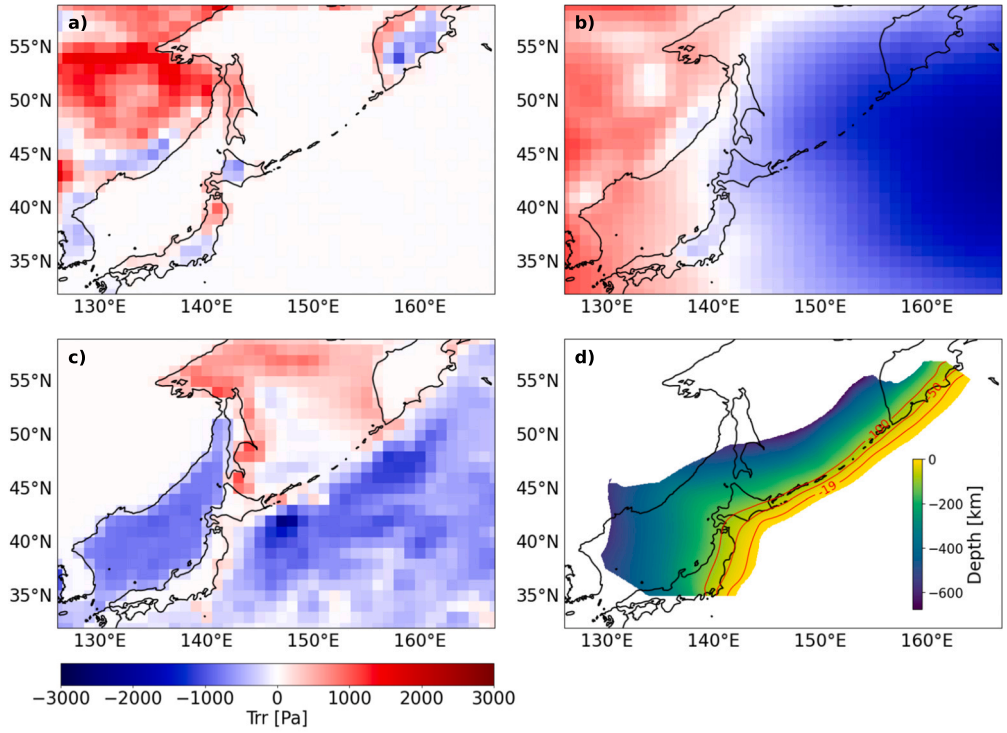

Fig. 1. Examples of the T_{rr} component of the stress tensor at 50 km depth in January 2011 and the geometry model used in the study. a) T_{rr} due to hydrological loading, b) T_{rr} due to atmospheric loading and c) T_{rr} due to non-tidal ocean loading, where the color bar is for all three T_{rr} plots of different surface loading in a, b, and c. d) The map of the studied subduction zone in the Kamchatka-Kuril Islands-Japan region.

and the 12-year earthquake catalog of the Kuril Islands-Japan region from 2005 to 2016. We then describe how we compute ΔCFF on the Kuril megathrust over the same time period, as well as the statistical method we use to compare it to the earthquake occurrence. We eventually present and discuss the results of our computations.

2. Data

The purpose of this study is to assess the correlation between seismicity and loading-induced Coulomb stress changes (ΔCFF), i.e. the stress induced by spatio-temporal redistributions of continental water (hydrological loading) and surface air pressure (atmospheric loading), and by non-tidal sea-level variations (non-tidal ocean loading). Computing ΔCFF requires information on the stress field and fault geometry, while seismicity data will be obtained from an existing database. In the following sections, we describe each of these components in detail.

2.1. Stress variations

For the hydrological and atmospherical loading-induced stress variations, we use the stress tensors computed by Lu et al. (2018). For the non-tidal ocean loading stress, however, we adopt another method. Below we describe each computation.

2.1.1. Hydrological and atmospheric loading

The loading-induced stress variations delivered by Lu et al. (2018) were computed for the compressible and elastic Gutenberg-Bullen A Earth model (Alterman et al., 1961). The data is provided as a stress tensor $\bar{\bar{T}}$ with six independent components $[T_{rr}, T_{r\theta}, T_{r\phi}, T_{\theta\theta}, T_{\theta\phi}, T_{\phi\phi}]$ in the geographical reference system $r-\theta-\phi$, where r is the radius, θ is the colatitude and ϕ is the east longitude. The stress variations due to the surface loadings are given at four representative depths, 0 km, 19 km, 50 km, and 100 km with a spatial resolution of $1^\circ \times 1^\circ$ and a temporal resolution of 1 month.

The stress variation due to the hydrological loading (Fig. 1a) is computed from terrestrial water storage (TWS) values estimated from the Global Land Data Assimilation System (GLDAS, Rodell et al., 2004), including contributions from soil moisture and snow, but not surface waters and groundwater below 2 m depth. Lu et al. (2018) also provide hydrological loading stress tensors computed from the observations of the GRACE satellite mission (Tapley et al., 2004), which tracks changes in the earth's gravity field since 2002. By design, GRACE monitors all water mass redistribution in the crust and should therefore provide a more complete hydrological load than GLDAS, which misses groundwater and various surface water components (such as rivers and lakes). The first reason why we don't use GRACE-derived stress tensors in this study is that the quality of the products decreased after 2010, while our study runs until 2016. The second reason is that the GRACE products used by Lu et al. (2018) integrate gravity changes coming from various different sources, including coseismic and postseismic effects which will yet be assimilated as hydrological loads. As our area of interest experienced the M_w9.1 Tohoku earthquake (11 March 2011), which displays large co- and post-seismic effects (e.g. Ozawa et al., 2011; Wang et al., 2012), we choose not to use GRACE-derived hydrological loading for this study.

The atmospheric-loading-induced stress variation (Fig. 1b) is derived from daily global pressure fields generated by the European Centre for Medium-Range Weather Forecasts (ECMWF). Note that the atmospheric-loading-induced stress variation is calculated with the atmospheric pressure applied directly on the seafloor, i.e. excluding sea level variations due to atmospheric pressure.

2.1.2. Non-tidal ocean loading

The non-tidal ocean loading as computed by Lu et al. (2018) is based on satellite altimetry data which is affected by sea water mass variations and steric effects. However, steric effects do not change the ocean bottom pressure and therefore should not be accounted for in the loading. Therefore, we computed the non-tidal ocean loading (Fig. 1c) using non-tidal ocean bottom pressure provided by the Estimating the

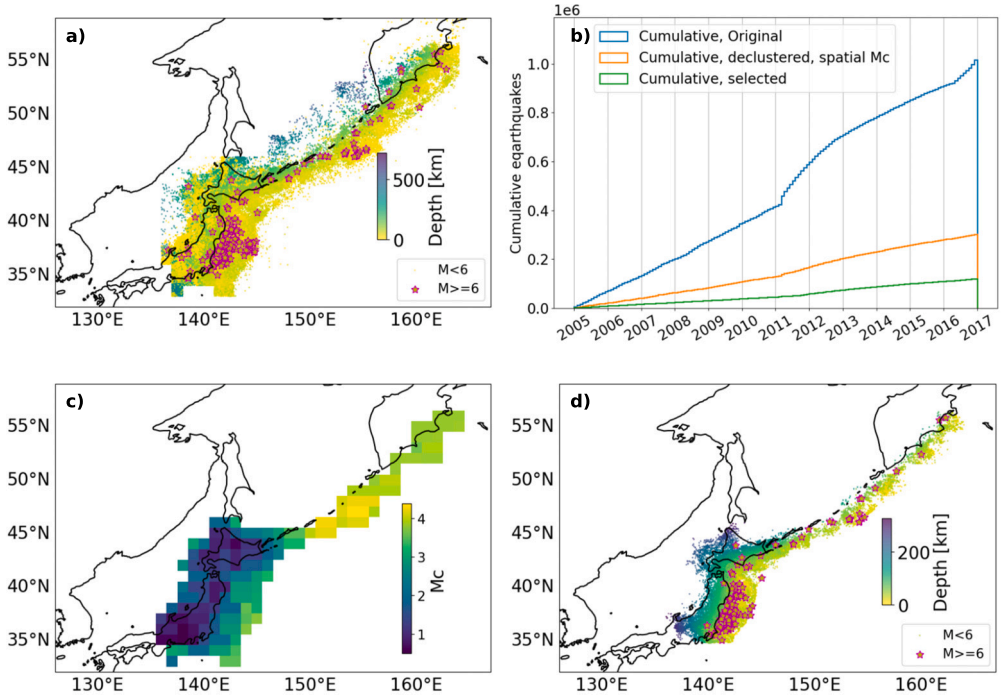

Fig. 2. a) Hypocenters of the 1016535 earthquake events in the original catalog. b) The cumulative seismicity of the original catalog, the declustered catalogs after removing the events with a magnitude below the local Mc, and the selected events that are within 32 km of the Kuril megathrust. c) Magnitude of completeness Mc on a 1° grid. d) Hypocenters of the 119753 selected earthquake events.

Circulation and Climate of the Ocean (ECCO) consortium (Menemenlis et al., 2008), with global and temporal averages removed (Martens, 2016). We first computed the strain tensors induced by these non-tidal ocean mass variations using the convolution scheme implemented in the tool LoadDef (Martens, 2016) and depth-dependent strain loading Green's functions computed using TidalStrain (Hirose et al., 2019; Hirose, 2023). The strain tensors hence obtained were then converted into stress tensors using Hooke's law and the Lamé parameters (λ, μ) given by the Gutenberg-Bullen A Earth model, as in Lu et al. (2018) and at the same representative depths as Lu et al. (2018), namely 0, 19, 50 and 100 km.

2.2. Subduction zone model

Subduction zones are the habitat of the most seismically active faults on the planet (Heuret et al., 2011). The Kamchatka-Kuril Islands-Japan region, where the Pacific plate is subducted under the Okhotsk plate, is one of the most earthquake-prone areas in the world (Warren et al., 2015). We will refer to the fault system in this region as the Kuril megathrust for short in the following texts.

The fault model used in this study is the Slab2 subduction zone geometry model (Hayes et al., 2018). It provides the following fault parameters: depth, strike, dip, average rake, thickness, and their respective uncertainties, with a spatial resolution of $0.05° \times 0.05°$. We use the depth (Fig. 1d), strike (Fig. S1b), dip (Fig. S1c), and average rake (89°) in our computation to project the stress tensors onto the Kuril megathrust. The depth uncertainty of the Slab2 model is used as the distance threshold for seismic event selection to locate the earthquakes belonging to the slab. More details will be given in Section 3.

2.3. Seismicity catalog

We use the ISC bulletin database (International Seismological Centre, 2023) to retrieve the seismic activities in the Kamchatka-Kuril Islands-Japan region between 2005 and 2016, totaling 1016535 earthquakes with a defined magnitude. Fig. 2a displays the hypocenters of the earthquakes and the blue curve in Fig. 2b is the cumulative earthquake numbers at a monthly scale. The ISC catalog contains the data contributed by several local agencies in the area, among which the Japan Meteorological Agency (JMA) is the primary contributor with 95% of the reported data. In Fig. 2b, there are two clear discontinuities in the original catalog, one in 2011 and one in 2016. The former is due to the influence of the 2011 Tohoku earthquake on the seismicity in the region (Hirose et al., 2011) and the latter is explained by the adoption of an auto-hypocenter-detection approach of JMA, which doubles the detected earthquakes in the catalog (Tamaribuchi, 2018).

As we aim to compare mainshocks occurrence to loading-induced ΔCFF, a prerequisite is to identify the magnitude of completeness Mc and to decluster the catalog. Following Johnson et al. (2017), given the large area covered by the earthquake catalog, we first assess the spatial variations in the magnitude of completeness (Mc) on $1° \times 1°$ grid patches (Fig. 2c). Mc is computed with a maximum-curvature method with a magnitude correction factor of 0.2 (Woessner and Wiemer, 2005) for all the earthquakes in the catalog. Mc is around 1 in the densely monitored areas in inland Japan and increases up to 3 in the offshore regions along the Japan trench, and it further reaches 4.4 along the Kuril trench. All further analyses of seismicity will be done within these grid patches, using their respective Mc.

Next, we decluster the ISC catalog to remove spatiotemporal densely clustered events, hence minimizing the dependency among the seismic activities. Indeed, clustered seismicity is mostly considered as tectonic driven (e.g. Stein, 1999; Toda et al., 2012; Chen et al., 2012), while we want to infer the triggering of earthquakes by surface loads, which are non-tectonic processes. This declustering is done using the Gardner-Knopoff algorithm (Gardner and Knopoff, 1974) with the Uhrhammer space-time proxy window (Uhrhammer, 1986) as implemented in the MATLAB package ZMAP (Wiemer, 2001).

The last step of the data preparation is to select earthquakes that occurred on the Kuril megathrust since their occurrence will be compared to the ΔCFF computed on that fault. They are chosen based on their distance to the slab model. The distance threshold of 32 km is chosen because it is the maximum depth uncertainty of the Kuril megathrust

specified in the *Slab2* model. There are 301714 earthquakes left after the declustering process and Mc cutoff and, among them, only the ones within 32 km of the Kuril megathrust are selected for further analysis.

Eventually, 119753 earthquakes with a magnitude greater than their local Mc are classified as independent earthquakes occurring on the Kuril megathrust, that is, about 40% of the declustered events. The majority of earthquakes are located along the Kuril Trench and the Japan Trench, and their hypocenters are presented in Fig. 2d. 80% (98530/119753) of the selected earthquakes in the studied region are located between 10 and 80 km depth, with the highest spatial density between 30 and 50 km depth. The large-magnitude ($M \geq 6$) earthquakes are rare and mostly distributed in the offshore Japan trench, while earthquakes with magnitudes between 1 to 3 represent more than 80% (97720/119753) of the whole earthquake population. More details of the depth and magnitude of the earthquakes are shown in Fig. S2.

3. Methods

3.1. Coulomb stress change

Coulomb stress change (ΔCFF) quantifies whether a fault is getting closer to or further from rupture when subjected to a given stress condition (King et al., 1994). It is thus commonly used to infer the influence of various processes, such as earthquakes (Lin and Stein, 2004), tides (Cochran et al., 2004), sediment redistribution (Steer et al., 2014) or other surfaces loads (Luttrell and Sandwell, 2010; Johnson et al., 2017), on the seismic hazard.

ΔCFF can be expressed as $\Delta CFF = \Delta\tau - \mu'\Delta\sigma_n$ (e.g. King et al., 1994; Stein, 1999), where the terms $\Delta\tau$ and $\Delta\sigma_n$ represent the changes in shear and normal stress on the fault, respectively, and μ' is effective friction coefficient, introduced under the assumption that the change in pore pressure in the fault zone is proportional to the normal stress (King et al., 1994; Harris, 1998). The stresses $\Delta\tau$ and $\Delta\sigma_n$ are derived from the monthly, depth-dependent stress variation tensors provided by Lu et al. (2018), and we set $\mu' = 0.4$, following King et al. (1994).

To compute ΔCFF, we first convert the stress tensor from the $r-\theta-\phi$ coordinate system (as given by Lu et al., 2018) to the North-East-Depth system, then define the fault plane coordinate system based on the fault geometry (strike and dip), project the stress tensor onto the fault base vectors to obtain the shear and normal stresses, and finally project the shear stress onto an axis parallel to the fault's rake (the shear stress will be maximal and positive if oriented in the same direction as the fault's rake). All the coordinate systems used are right-handed. Also, as outlined in Section 2.1, the stress tensors are provided at four depths (0, 19, 50, and 100 km), which we select according to the depth at which ΔCFF is computed. For example, if the fault depth falls within the range of [0 km, 19 km), including 0 km but excluding 19 km, we use the stress tensor at 0 km, $\bar{\bar{T}}(0)$, for our calculations.

We eventually sum the individual Coulomb stress change associated with each loading source: $\Delta CFF = \Delta CFF_{hydro} + \Delta CFF_{atmos} + \Delta CFF_{NTO}$, to obtain the total, loading-induced, ΔCFF on the Kuril megathrust. Note that ΔCFF has the same spatial resolution as Slab2, that is $0.05° \times 0.05°$. However, the fault parameters from Slab2 exhibit little variation at this scale (Fig. 3a-d), and the spatial resolution of ΔCFF looks largely controlled by the spatial resolution of the stress field (1°). An example of the Coulomb stress change throughout 2011 on the Kuril megathrust is presented in Fig. 3e.

3.2. Comparison to seismicity

To identify areas where the surface-load-induced stress changes potentially influence earthquake occurrence, we investigate the correlation between ΔCFF and earthquake occurrence by comparing the time series of the ΔCFF and the seismicity in each of the $1° \times 1°$ grid patches where M_c was evaluated.

An example of a patch and its associated time series is shown in Fig. 4. In each patch, we compare the areal mean ΔCFF to the excess (or deficiency) of seismicity R_{ex} at each month in 2005-2016. The areal mean ΔCFF(t) is computed by averaging all the ΔCFF(t) values within the patch. This is acceptable because we have seen in Section 3.1 that ΔCFF is largely controlled by the spatial resolution of the stress field (1°) and does not show large variability within each patch.

The excess (or deficiency) of seismicity $R_{ex}(t)$ is express as a percentage and computed as: $R_{ex}(t) = \frac{N_{tot}(t) - N_{mean}}{N_{mean}} \times 100$ where $N_{tot}(t)$ is the total number of selected earthquakes in the patch for a given month and N_{mean} is the monthly mean number of earthquakes per month from 2005 to 2016. Our hypothesis is that the average seismicity over the entire period of study represents the fault's response to static tectonic stress, and the deviation from this mean value is the result of surface-loading-induced stress. Therefore, a positive correlation between $\Delta CFF(t)$ and $R_{ex}(t)$ in a given patch indicates that more earthquakes are associated with loading-induced stress variations in the area, and vice versa.

We then infer the correlation between the loading-induced stress on the Kuril megathrust and its seismicity variations by computing the Spearman correlation coefficient between ΔCFF(t) and $R_{ex}(t)$. Spearman correlation enables us to calculate the correlation coefficient between the rank of ΔCFF(t) and $R_{ex}(t)$ at each patch to investigate the monotonicity of the relationship between ΔCFF(t) and $R_{ex}(t)$. We only consider patches where $N_{mean} \geq 3$, i.e. where at least 216 background earthquakes occurred between 2005 and 2016, to have adequate data for statistical analysis. This threshold is an empirical choice because a value lower than such a threshold leads to a falsely high correlation even with the randomized catalogs.

3.3. Statistical significance test

Here we describe how we assess the statistical significance of our findings. We define a null hypothesis that states that loading-induced stress variations do not affect earthquake occurrence in the region, meaning that R_{ex} are independent of ΔCFF, and evaluate in which patches the null hypothesis can be rejected.

We first generate 500 independent test catalogs by randomly reassigning timestamps to every earthquake in the analyzed catalog. The locations of these earthquakes and their total amount remain identical to the analyzed catalog. Timestamps are uniformly distributed within the same time range as the real earthquake catalog, that is between 2005-01-01 00:00:00 and 2016-12-31 23:59:59. These random time reassignments ensure that these earthquakes also occur at random times from the loading-induced ΔCFF(t), meaning that the null hypothesis holds for all of them.

We then repeat the methods described in Section 3.2 to compare the randomized $R_{ex}(t)$ with the $\Delta CFF(t)$ and record the output for each test. With the generated 500 test catalogs, the Spearman correlation coefficients are normally distributed around 0, and thus we can utilize a two-sided z-score to test the statistical significance of the correlation coefficients between the observed $R_{ex}(t)$ and the ΔCFF(t). The z-scores are then converted to p-values and we deem a p-value smaller than 0.05 as significant, indicating rejection of the null hypothesis with 95% confidence. Therefore, areas with a p-value smaller than 0.05 and a positive correlation coefficient are considered to have their seismicity enhanced by the combination of atmospheric, hydrological, and non-tidal ocean loadings.

4. Results

4.1. Loading-induced Coulomb stress change

Fig. 5 shows examples of loading-induced ΔCFF(t) at three different locations on the Kuril megathrust with hydrological loading, atmospheric loading, and non-tidal ocean loading as the main contributor, respectively. The multi-loading-induced ΔCFF on Kuril megathrust is the

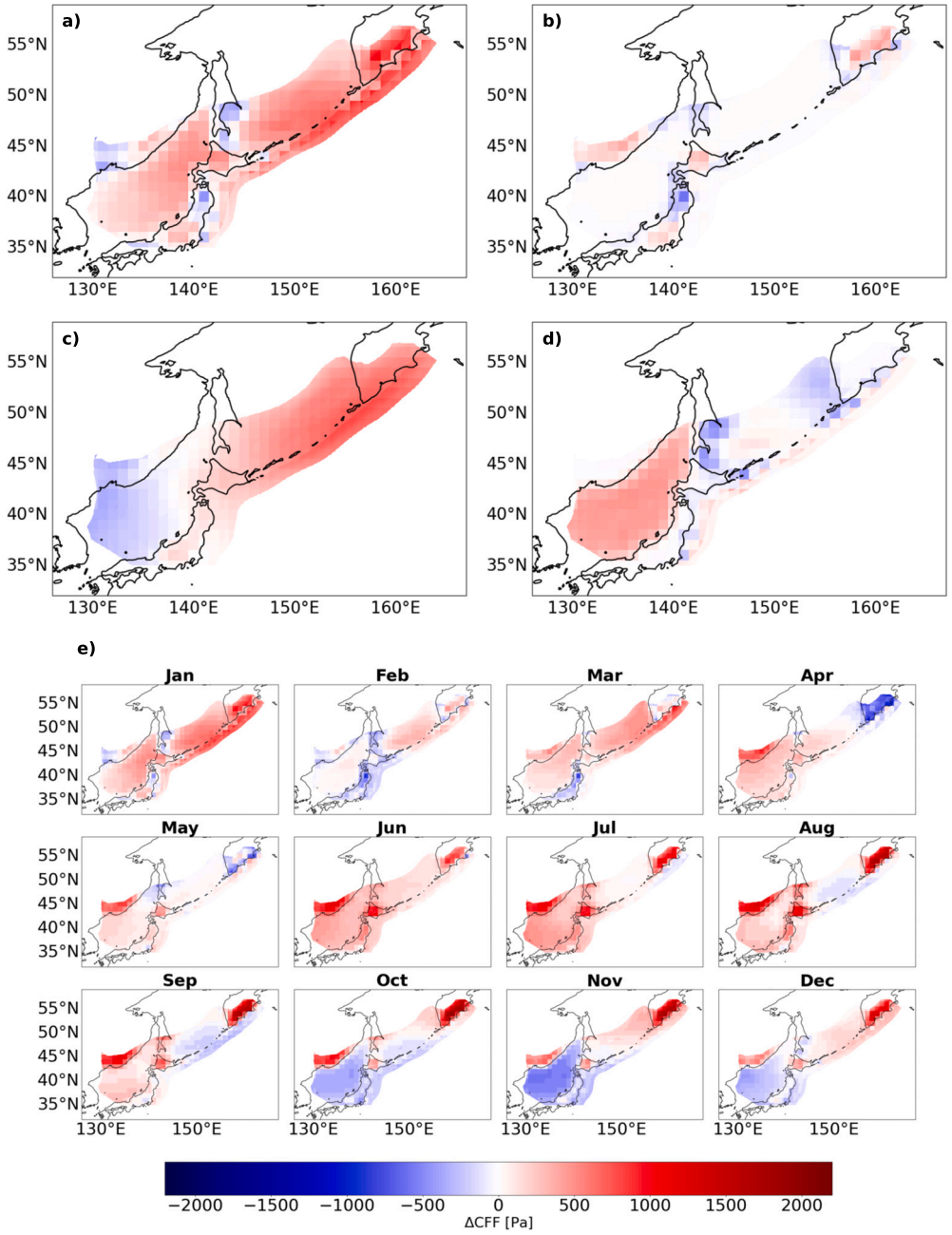

Fig. 3. Bird's-eye view of ΔCFF on the Kuril megathrust in January 2011 under the surface loads considered in this study. a) Total loading-induced Δ CFF, b) ΔCFF_{hydro} due to the hydrological loading, c) ΔCFF_{atmos} due to the atmospheric loading, and d) ΔCFF_{NTO} due to non-tidal ocean loading. e) Monthly maps of the total loading-induced ΔCFF in 2011.

combination of the corresponding single-loading-induced $\Delta\text{CFF}_{loading}$. The slab beneath the land area at 158°E, 54°N (Fig. 5b) is predominantly influenced by hydrological loading. The stress variations on the deep slab in the Sea of Japan at 138°E, 40°N (Fig. 5c) are mainly contributed by non-tidal ocean loading and partly by atmospheric loading, whereas the shallow slab in the oceanic area at 143°E, 39°N (Fig. 5d) is primarily influenced by atmospheric loading among the three surface loadings. We also observe that both the ΔCFF time series at 158°E, 54°N in Fig. 5b and 143°E, 39°N in Fig. 5c display seasonality (1 year period) but with different amplitudes and temporal patterns. The former ΔCFF is generally low during spring in most studied years with peaks appearing between July and October, while the latter ΔCFF peaks earlier between April and July, and shows a trough in winter bottoming around December. However, as shown in Fig. 5c, the periodicity in the ΔCFF of 138°E, 40°N is not as clear as of the other locations, especially after 2008. The variation in the periodicity of ΔCFF across the study area will be discussed in Section 5.1.

We also compute the peak-to-peak amplitude of ΔCFF(t) across the study area depicted in Fig. 6a, representing the difference between the highest and lowest values during the study period. The shallow edge of the Japan Trench experiences the lowest amplitude at 0.8 kPa. The slab beneath the Kamchatka Peninsula experiences the highest amplitude, reaching about 4 kPa. Notable variations of amplitude are also observed in the slab surface under Hokkaido Island and the northwestern rim of the Sea of Japan. Overall, the total loading-induced ΔCFF ranges within a few kPa. Despite being a rather modest stress variation compared to the eventual stress drop released by earthquakes (typically 1 - 10 MPa),

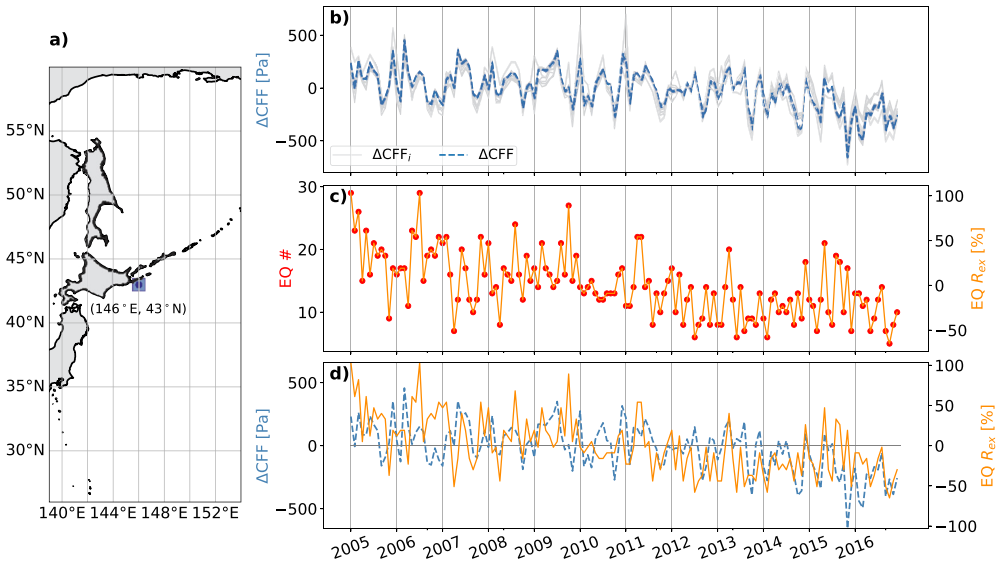

Fig. 4. Comparison of the ΔCFF and the percentage of excess (or deficiency) earthquakes time series for the 1° × 1° patch located at 146°E, 43°N. a) The location of the example patch. The continental areas are shaded in gray. b) Time series of the ΔCFF. The gray lines are the ΔCFF_i of all the grids at a spatial resolution of 0.05° located within the 1° × 1° patch, totaling 400 grids, and the blue dashed line represents the areal mean $\Delta CFF(t)$. c) Percentage of excess (or deficiency) earthquakes time series ($R_{ex}(t)$). The red dots stand for $N_{tot}(t)$ the number of earthquakes that occurred within the patch each month, and the orange line is $R_{ex}(t)$. d) Superposition of b) and c).

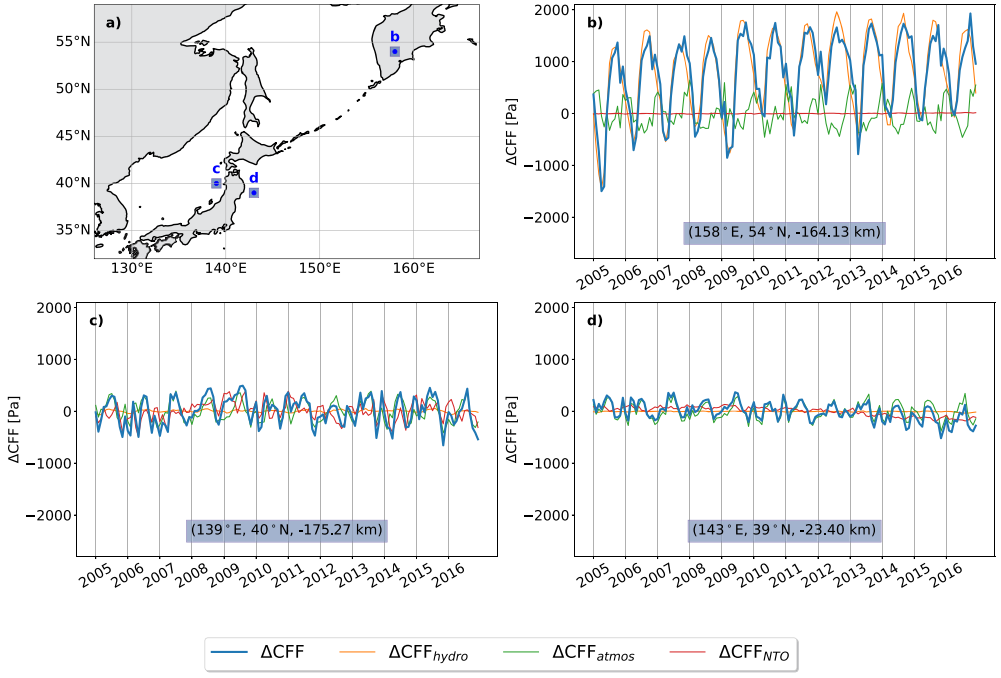

Fig. 5. ΔCFF at three example locations, marked with blue squares in a), with different surface loadings as their primary loading. The continental areas are shaded in gray. b) 158°E, 54°N, hydrological primary loading peaks in autumn and bottoms in spring, c) 131°E, 42°N, atmospheric primary loading peaks in late spring and early summer while notch in winter, and d) 143°E, 39°N, non-tidal ocean primary loading roughly peaks in spring and summer and bottoms in winter, but the amplitude varies dramatically from year to year.

this remains sufficient to alter the secular tectonic stress build up in Japan, estimated at a few tens of kPa per year (Heki, 2003).

By comparing the amplitude of each loading component, we also evaluate which of the atmospheric, hydrological, or non-tidal ocean loading has the largest influence in each grid patch (Fig. 6b). The primary loading varies across each location and appears to be associated with geographical settings. Hydrological loading represents the largest contributor to ΔCFF on most of the slab region located beneath the land. In the majority of oceanic areas, atmospheric loading contributes the most to ΔCFF, especially in the shallow portion of the Kuril megathrust along the Japan Trench and Kuril Trench. Only in the area under the eastern Sea of Japan, the non-tidal-ocean loading is the primary source of ΔCFF. Therefore, given the pronounced variability in primary loading across our study area, we suggest that examining the cumulative effect of multiple loading factors is important when evaluating the influence of surface loads on seismicity.

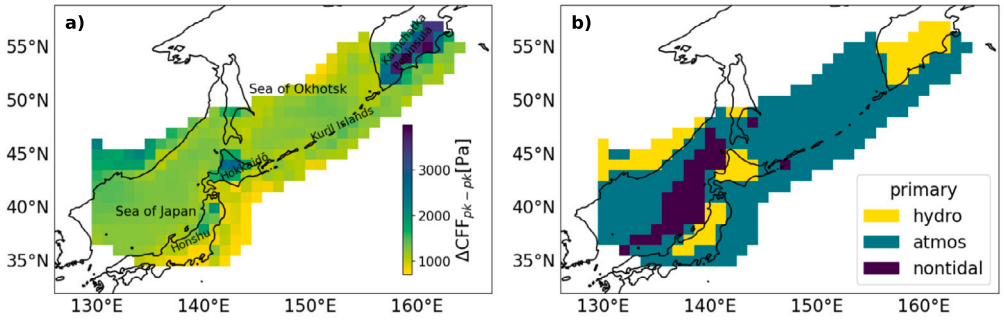

Fig. 6. a) The peak-to-peak ΔCFF and b) the primary loading process on the plate interface. All plots are in a bird's-eye view of the Kuril megathrust.

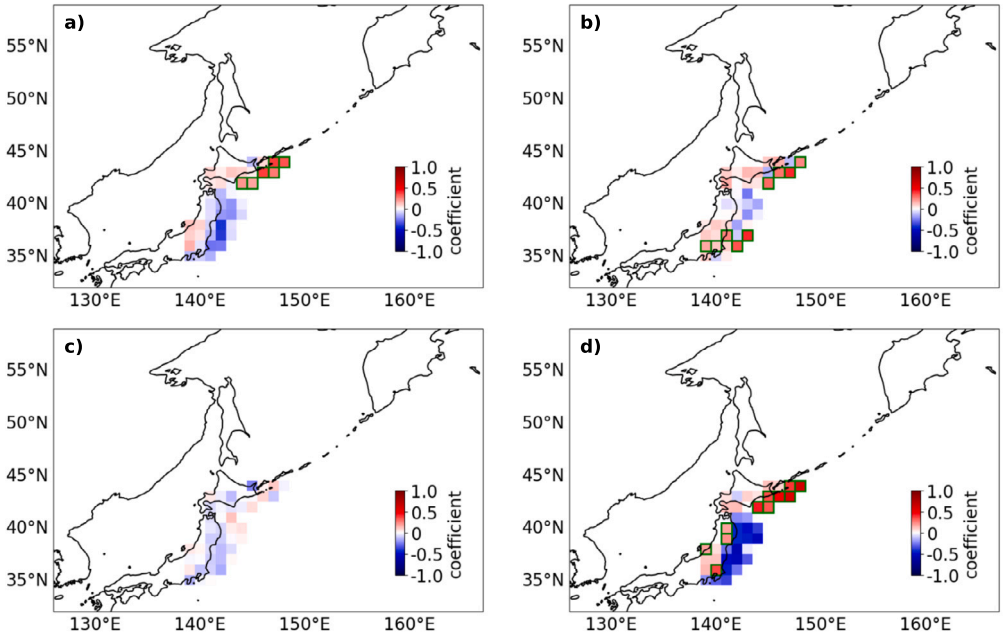

Fig. 7. Correlation coefficients between a) multiple surface-loading-induced Coulomb stress change ΔCFF and R_{ex}, b) the hydrological-loading-induced Coulomb stress change ΔCFF_{hydro} and R_{ex}, c) the atmospheric-loading-induced Coulomb stress change ΔCFF_{atmos} and R_{ex} and d) the non-tidal ocean loading induced Coulomb stress change ΔCFF_{NTO} and R_{ex}. Hot zone patches with a statistically significant positive correlation are highlighted with green bounding boxes.

4.2. Comparison of $\Delta CFF(t)$ with $R_{ex}(t)$

We now quantitatively evaluate the impact of surface loading processes on seismic activity by assessing the correlation of the $\Delta CFF(t)$ with the excess (or deficiency) earthquake rate $R_{ex}(t)$. The analyzed areas cover the shallow portion of the Kuril megathrust along northeastern Honshu Island and eastern Hokkaido Island and extend to the slab beneath these islands. The area along the Kuril Trench from Kamchatka Penisula to the southern Kuril Islands is eventually not part of the analysis due to the lack of earthquakes.

The correlation coefficients are mapped in Figs. 7a, where the outstanding patches with a positive correlation coefficient and a p-value smaller than 0.05 are highlighted with green bounding boxes. They correspond to areas where the seismicity is enhanced by the increase of loading-induced ΔCFF, or conversely. One region stands out in Fig. 7a, a cluster of six patches off the east shore of Hokkaido Island at the southern Kuril Trench around 146°E, 43°N. Hereafter, this area is called the $Hokkaido$ hot zone. The correlation coefficients range from 0.2 to 0.4, meaning that this correlation is weak as per the convention proposed by Schober et al. (2018). The correlation coefficients, their corresponding p-value, the statistic tests, and the time series of ΔCFF and R_{ex} of all outstanding patches of the Hokkaido hot zone can be found in the supplementary material (Fig. S3, and Fig. S4). Among the six patches, five are located between 15 km and 35 km depth, with one patch located at 147°E, 44°N reaching a depth of 57 km (Fig. S4).

The primary loading source is the atmosphere in the Hokkaido hot zone (Fig. 6b). The peak-to-peak amplitude of ΔCFF is around 1 kPa for the Hokkaido hot zone (Fig. 6a), which indicates the local fault systems are critically stressed and extremely sensitive to small stress perturbations. This is consistent with previous studies in the Himalayas (Bettinelli et al., 2008) and California (Christiansen et al., 2007; Gao et al., 2000), which also revealed correlations between seismic activity and small stress perturbations (a few kPa) resulting from the surface loading.

When comparing ΔCFF_{hydro}, ΔCFF_{atmos}, and ΔCFF_{NTO} with respect to R_{ex} in the region (Fig. 6b-d), we can once again see the importance of examining the cumulative effect of multiple loading factors. The inconsistency between the single-loading results and multi-loading results indicates that drawing conclusions from an analysis of one single-loading source can be risky. Given that, in reality, all these loading factors act on the fault simultaneously, relying solely on numerical outcomes from a single loading analysis is potentially inaccurate. For instance, when examining only hydrological loading, there are two hot zones in Fig. 7b one in the northern Kuril megathrust and one spanning from the shallow Japan Trench to the inland Honshu Island in the southern Kuril megathrust. However, the pronounced significant positive correlation in the latter hot zone almost entirely diminishes

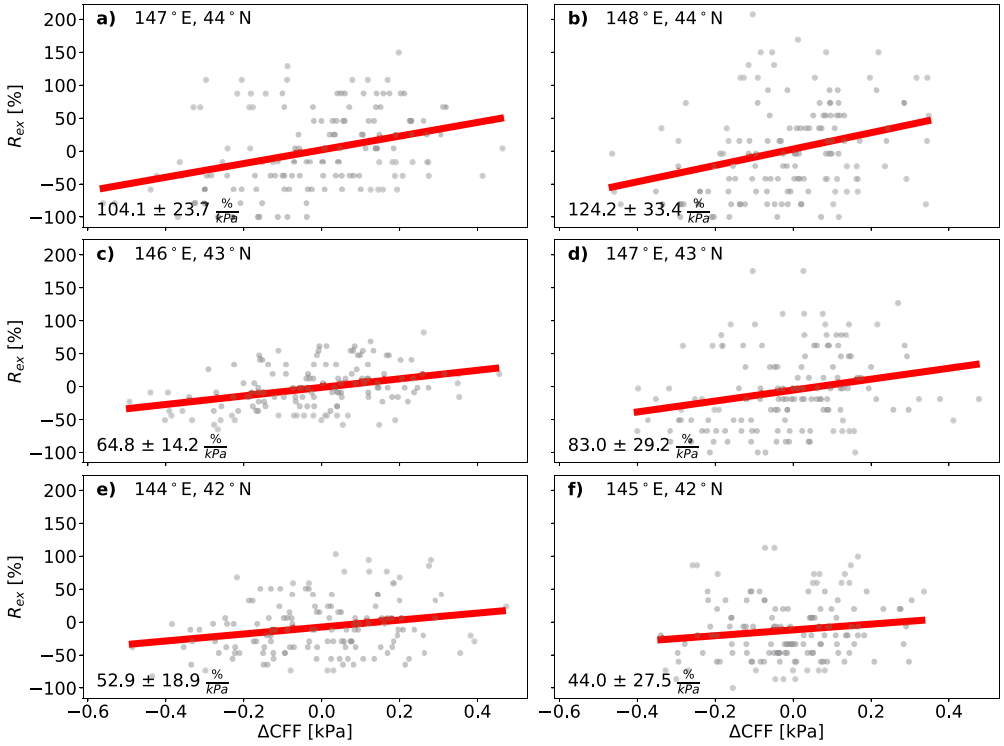

Fig. 8. The excess (or deficiency) earthquake rate in percentage R_{ex} versus the loading-induced Coulomb stress change ΔCFF ($\mu = 0.4$) for the six patches of the Hokkaido hot zone. The gray dots in the background are the monthly data of the ΔCFF and R_{ex} between 2005 and 2016 at each location. The best-fit line of the gray dots is plotted in red and its slope is shown in the lower-left corner of each plot with the standard error.

in Fig. 7a when considered together with non-tidal ocean loading and atmospheric loading. Also, when comparing the seismicity with only non-tidal-ocean loading, the correlation coefficients for the Hokkaido hot zone are over 0.6, which is substantially higher than the ones from the multiple-loading analysis. Therefore, we suggest that reliable results are best obtained through a comprehensive multi-loading analysis when studying the areas exposed to various loadings.

In Fig. 8, the percentage excess (or deficiency) earthquake rate R_{ex} is plotted against the loading-induced ΔCFF ($\mu' = 0.4$), for the Hokkaido hot zone. The red lines represent the best-fit lines of the gray data points, and the slope of each best-fit line is presented in the lower-left corner of the plot along with its standard error. The regression line represents the best-fit linear relationship between the ΔCFF and R_{ex} over 12 years between 2005 and 2016 at the six outstanding patches of the Hokkaido hot zone. The slope of the best-fit lines varies from $44.0\%/kPa$ up to $124.2\%/kPa$, with a mean slope of 78.8%/kPa across the entire hot zone. The slope of the observed relationship increases with higher latitude values, indicating that patches situated further north in the study area demonstrate a greater variation in R_{ex} per unit change in ΔCFF. However, the interpretation of these slopes should be approached with caution given that the correlation coefficients are below 0.4. Nonetheless, the spatial coherence and consistent pattern of the hot zone patches suggest the correlation is likely a real feature.

5. Discussions

5.1. Periodicity of surface loads and seismicity

Although surface loads are often found to display a seasonal pattern, Fig. 5 shows that this assumption is not always valid when combining different load processes. In Fig. 5b and d, ΔCFF(t) reaches local maxima with a periodicity of about 1 year, which is controlled by the periodicity of the surface loads. However, such a 1-year period is not clear in Fig. 5c which shows stress deep in the subducting slab under the Japan Sea. This observation is further corroborated by the wavelet power spectrum plots depicted in Fig. S5. In addition, Fig. 9 shows that ΔCFF(t) is not periodic in most of the Hokkaido hot zone. Only Fig. 9a (location 147°E, 44°N) displays a 1-year periodicity between 2007 and 2012. The ΔCFF observed along the Kuril megathrust, which is affected by multiple sources of surface loading, exhibits location-dependent temporal patterns. Similarly, we do not observe clear periodicity in the background seismicity declustered with the GKUH method (Fig. S6) or the nearest-neighbor declustering method (Fig. S7). Despite the variability in seasonality of both surface loads and seismicity in the Hokkaido hot zone, we observe statistically significant correlations between the stress variation of surface loads and seismicity at all the hot zone areas. This suggests that in areas where the surface loadings and earthquakes are not periodic, the stress changes associated with the loading can still have a significant impact on temporal variations in the background seismicity. At the locations exposed to multiple load sources, the combined surface loads may not always be periodic, hence a purely frequency-based study of seismicity may miss some actual correlation between surface loads and seismicity. Thus, we suggest that analyzing continuous data of the aggregated load history spanning the entire observational period is necessary when investigating the impact of multiple surface loads on seismicity.

5.2. Limited instantaneous seismic responses to hydrological loading

Our result suggests the seismicity in most slab areas deeply (>50 km) beneath the inland area, where the hydrological loading is the primary loading, generally does not correlate with loading-induced ΔCFF. We restricted our analysis to instantaneous correlations, comparing ΔCFF and R_{ex} for the same months. Similarly, in southern Alaska, (Johnson et al., 2020) also observed limited instantaneous seasonal-loading seismic modulation but inferred that the increase of regional seismicity rate lagged the peak stress conditions by three months. They proposed a time-delayed hydrological-loading triggering mechanism, possibly controlled by the change in crustal pores. Other examples of such delayed

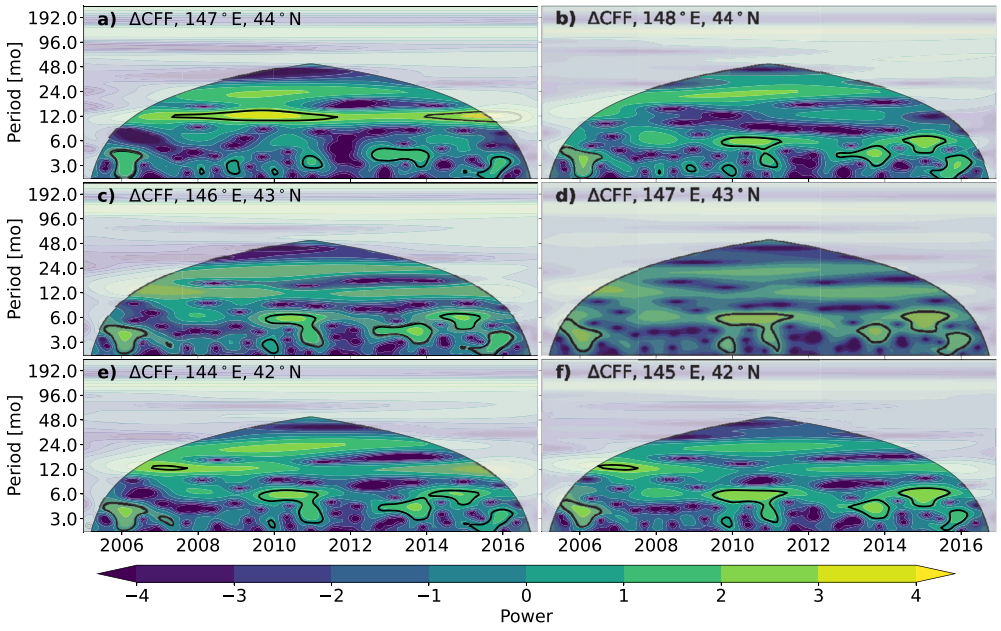

Fig. 9. The wavelet power spectrum of the time series of ΔCFF by applying the continuous wavelet spectral analysis for the Hokkaido hot zone. The high power period is highlighted in yellow and the black contours mark the 95% significance level. The shaded white regions lie outside the cone of influence where the edge effect reduces the certainty.

modulations have been observed in Taiwan (3-5 months delay, Hsu et al., 2021), and the Himalayas (days-to-months delay, Bettinelli et al., 2008). In this study, we do not investigate the degree of delayed triggering in the region.

5.3. Data uncertainty

One limitation of this study pertains to the spatial and temporal resolution of the loading-induced stress variation data we used. The available stress fields are provided at discrete depth intervals, specifically at characteristic depths of 0 km, 19 km, 50 km, and 100 km, as outlined in Lu et al. (2018). Consequently, the computation of ΔCFF on the fault systems relies on these depth intervals, possibly leading to inaccurate values. To enhance the precision of our analysis, future endeavors would benefit from computing the loading-induced stress tensors with a finer depth sampling. This is made possible for instance by the recent work of Hirose et al. (2019) and Hirose (2023), who provide tools to compute depth-dependent load Green functions at arbitrary depths.

5.3.1. GLDAS and GRACE

When it comes to the hydrological loading, we explained in Section 2.1 that the GRACE-derived stress tensors published by Lu et al. (2018) were both too short in time and subjected to significant co- and post-seismic effects from the Tohoku earthquake, and thus not being ideal for our study. Here we assess the implication of this choice by making a comparative analysis of seismic activity results spanning the years 2005 to 2010, using either GRACE- or GLDAS-derived hydrological stress tensors. By ending the comparison in 2010 we ensure that the GRACE-derived stress variations are both complete (2010 is the last year for which complete 12-month data is available) and not affected by the Tohoku earthquake. As depicted in Fig. S8a and b, it becomes evident that the relationship between R_{ex} and GLDAS-derived ΔCFF_{hydro} differs noticeably from that of the GRACE-derived counterpart. However, this disparity diminishes when combining hydrological loading with non-tidal ocean loading and atmospheric loading (Fig. S8c and d). The histogram plot in Fig. S8e provides additional confirmation of this observation. It highlights differences in the correlation coefficients between R_{ex} and GLDAS-derived ΔCFF_{hydro} when compared to those between R_{ex} and GRACE-derived ΔCFF_{hydro} of up to 0.4, while the differences between the multi-loading results mostly remain within the 0.1 range. One perspective for using GRACE products to compute hydrological-induced stress would be to use recently published solutions by Gauer et al. (2023) that aimed to fill all GRACE data gaps, including that from GRACE to GRACE Follow-on. One major advantage of GRACE data over global hydrological models is the fact that, as an observation, it properly captures the inter-annual ground water storage variations, including trends of water depletion extending over several years (e.g. Rodell et al., 2009; Wang et al., 2011). Such inter-annual patterns are notoriously difficult to retrieve in hydrological models (Scanlon et al., 2018). GRACE also contains information on groundwater storage variation, which is missing in global hydrological models.

5.3.2. Declustering algorithm

This study is constrained to analyze the complete catalog containing independent earthquakes located on the Kuril megathrust. The independent earthquakes are selected with the Gardner-Knopoff algorithm with the space-time window defined in Uhrhammer (1986). It is worth noting that various alternative declustering methods are available. One could use the original method introduced by Gardner and Knopoff (1974), the Reasenberg algorithm (Reasenberg, 1985), the nearest-neighbor method (Zaliapin and Ben-Zion, 2013), and other methods that have been developed in recent years. We repeat our analysis with the nearest-neighbor method and the original Gardner-Knopoff algorithm to evaluate the potential uncertainty in the results included by the declustering operation.

The additional analysis with the nearest-neighbor method does not change the conclusions we draw in Section 4.2, as illustrated in Fig. S9. The Hokkaido hot zone at the same locations as in Fig. 7a still stands out, except for slight changes of patches on the south edge of the hot zone. The displayed areas with correlation coefficients slightly vary due to the change in the catalog, some areas may contain adequate numbers of independent earthquakes in one test and may be excluded in another test if the number of independent earthquakes is too low. However, the hot zone identified using the original Gardner-Knopoff algorithm in Fig. S10a does exhibit differences from the preselected hot zone. These differences may be linked to the increased uncertainty arising from the utilization of a smaller population of events (40803) that have undergone declustering via the original Gardner-Knopoff algorithm, considering that the original Gardner and Knopoff windowing

might overestimate aftershocks, potentially leading to the removal of a significant number of events, as suggested by Barani et al. (2007). Nevertheless, the multi-loading result is still different from the single-loading results, which once again stresses the importance of a comprehensive analysis of multiple surface loadings.

5.4. Validity of the assumption of steady background loading

In this study, we assume that the background seismicity rate remains constant due to the influence of static tectonic stress, and thus, any deviations can be attributed to non-tectonic processes, such as stress variations induced by surface loading. This assumption invites scrutiny from two angles. Firstly, it relies on the hypothesis that background seismicity remains constant throughout the entire observational period, which becomes questionable, especially in the wake of great seismic events such as the 2011 Tohoku Earthquake. However, as illustrated in Fig. 2c, the cumulative number of eventually selected events (as indicated by the green line) does increase linearly over time, which assures that most of the aftershocks from the Tohoku earthquake have been properly removed from the catalog. In addition, postseismic deformation due to Tohoku earthquake (e.g. Ozawa et al., 2012; Fukuda and Johnson, 2021) and slow-slip events (Uchida et al., 2016; Nishikawa et al., 2019) may also influence both the stress and seismicity of the studied area. Secondly, the solid Earth tides and ocean tides also act simultaneously with the three non-tectonic loading sources we included in this study, but are not incorporated into the scope of our analysis. We discuss the role of the tectonic stress change rate, postseismic effects, slow earthquakes, and tidal loading in the following.

5.4.1. Tectonic stressing

The location and depth of the Hokkaido hot zone generally agree with the northern slip-deficit zone around 42-44°N, 143-147°E in the depth range of 10–40 km described by Hashimoto et al. (2009). Considering the potential dependence of the earthquake nucleation time on the stressing rate, and thus the susceptibility of seismicity to modulation (Ader et al., 2014), it may be worthwhile to conduct a more thorough comparison of the temporal and spatial variations in background stress rates within the area with the degree of modulation by loading-induced stresses of varying amplitude and period. Nevertheless, we note that the relationship between the rate of ΔCFF due to tectonic and non-tectonic loadings to seismic nucleation remains a subject of debate. Modulation of earthquakes due to surface-loading has been observed in regions with both low tectonic stress change rates, such as the New Madrid Seismic Zone (Craig et al., 2017), and high tectonic stress change rates, as seen in California (Johnson et al., 2017). Moreover, earthquakes of varying magnitudes or depths within the same area may exhibit differing responses to surface loading. For example, in northeastern Japan, Heki (2003) noted that the removal of snow load could increase ΔCFF on shallow faults and may trigger large inland earthquakes, though this pattern was not observed in small-magnitude earthquakes. Similarly, in eastern Taiwan, Hsu et al. (2021) suggested elastic hydrological load cycles as the primary driver for synchronized modulation of deep earthquakes (>18 km), while shallow earthquakes (<18 km) appear to be anticorrelated with water unloading.

5.4.2. Postseismic effects

Significant postseismic deformation occurred after the Tohoku earthquake (Ozawa et al., 2012). To assess the impact of such a large earthquake on our findings, we divide the data into two equal time periods: one from 2005 to 2010, excluding the Tohoku earthquake, and the other spanning from 2011 to 2016, including the event. No hot zones are detected in the results from 2005 to 2010 and from 2011 to 2016 (Fig. S11). We observed some positive correlations around the epicenter of the Tohoku earthquake at 38.296°N, 142.498°E but none are statistically significant. We note that the comparison here involves a halved time series of only 6 years, which increases the uncertainty of the correlation coefficients. Nevertheless, the Hokkaido hot zone identified in the 12-year analysis is not located in the afterslip area offshore of Honshu Island proposed by Ozawa et al. (2012) and Fukuda and Johnson (2021). This spatial separation suggests that the postseismic effects of the Tohoku earthquake are unlikely to have a substantial impact on our findings.

5.4.3. Slow earthquakes

In the Kuril Islands-Japan region, slow earthquakes and slow-slip events have also occurred. Such transient deformations are capable of episodically influencing seismicity on time scales longer than 1 month. However, distinguishing earthquakes triggered by slow earthquakes from those induced by surface loads remains a challenge. If the regions with frequent slow earthquakes coincided with those showing significant positive correlations in our study, it would suggest that slow earthquakes might enhance the seismic sensitivity of these areas to surface loads. But our identified hot zone in Fig. 7a is not located in the regions characterized by Uchida et al. (2016), or Nishikawa et al. (2019), or the locations of slow-slip events documented in the database developed by Kano et al. (2018). Therefore, we believe that the impact of slow slip deformation on our findings remains negligible.

5.4.4. Tidal loading

Tidal effects are not incorporated into the scope of our analysis because they operate on very short timescales, most of its components having sub-daily or daily periods. Based on laboratory experiments, Beeler and Lockner (2003) suggested that such short periods are the reason why several studies only find a weak influence of tides on earthquake triggering. The tidal stress, despite also reaching values of the order of several kPa, is not sustained long enough to promote the failure of faults, suggesting that the faults have a minimum typical duration of earthquake nucleation. Beeler and Lockner (2003) estimated a nucleation duration of about 1 year, and if we assume a duration of the same order of magnitude, we see that the surface-loading-induced ΔCFF time series computed in our study are better candidates than tides to trigger earthquakes. Nevertheless, the impact of tidal stresses on seismicity remains an active research area and different studies have evidenced the role of tides in earthquake modulation (Cochran et al., 2004; Rubinstein et al., 2008; Tanaka et al., 2023). Although beyond the scope of this study, where our analysis is based on monthly time intervals, integrating tidal processes would yield a more comprehensive budget of surface-loading-induced ΔCFF. Such an extension would offer a more accurate physical representation of the non-tectonic stresses exerted on the fault systems.

6. Conclusions

We find a relatively modest but significant positive correlation between earthquake occurrences and Coulomb stress changes induced by multiple surface loadings, including hydrological, atmospheric, and non-tidal ocean loadings, particularly within the shallow stretch of the Kuril megathrust along the southern Kuril Trench off Hokkaido. Notably, our research highlights the variability in primary loading across the expansive Kuril Islands-Japan subduction zone. We thus stress the necessity of considering a range of loading sources for regional stress variation studies, given that each loading source exhibits distinct temporal and spatial distributions. We also underscore that the Coulomb stress changes induced by multiple surface loadings do not adhere to consistently periodic patterns. Despite these loadings yielding relatively modest Coulomb stress changes up to an amplitude of a few kPa, their impact on seismic activity demonstrates statistical significance, which may not be noticed by solely analyzing a single loading source or a single (annual) loading period. Therefore, it is important to aggregate the contributions of various surface loadings to comprehensively investigate their collective influence on active fault systems and seismic activities.

CRediT authorship contribution statement

Yiting Cai: Writing – review & editing, Writing – original draft, Visualization, Validation, Resources, Methodology, Investigation, Formal analysis, Data curation. **Maxime Mouyen:** Writing – review & editing, Validation, Supervision, Resources, Project administration, Methodology, Funding acquisition, Formal analysis, Conceptualization.

Declaration of competing interest

The authors declare that they have no known competing financial interests or personal relationships that could have appeared to influence the work reported in this paper.

Data availability

Data will be made available on request.

Acknowledgements

The authors thank the editor Jean-Phillipe Avouac, and the reviewer Christoper. W. Johnson and one anonymous reviewer for their constructive comments and suggestions that improved the quality of the project and manuscript. The authors also deeply thank Roland Bürgmann and Kristel Chanard for their invaluable discussions and feedback. The authors thank Zhou Lu for clarification of the details of the public loading-induced stress data.

Appendix A. Supplementary material

Supplementary material related to this article can be found online at https://doi.org/10.1016/j.epsl.2024.118904.

References

Ader, T.J., Lapusta, N., Avouac, J.P., Ampuero, J.P., 2014. Response of rate-and-state seismogenic faults to harmonic shear-stress perturbations. Geophys. J. Int. 198, 385–413. https://doi.org/10.1093/gji/ggu144.

Alterman, Z., Jarosch, H., Pekeris, C., 1961. Propagation of Rayleigh waves in the Earth. Geophys. J. Int. 4, 219–241. https://doi.org/10.1111/j.1365-246X.1961.tb06815.x.

Barani, S., Ferretti, G., Massa, M., Spallarossa, D., 2007. The waveform similarity approach to identify dependent events in instrumental seismic catalogues. Geophys. J. Int. 168, 100–108. https://doi.org/10.1111/j.1365-246X.2006.03207.x.

Beeler, N., Lockner, D., 2003. Why earthquakes correlate weakly with the solid Earth tides: effects of periodic stress on the rate and probability of earthquake occurrence. J. Geophys. Res., Solid Earth 108. https://doi.org/10.1029/2001JB001518.

Bettinelli, P., Avouac, J.P., Flouzat, M., Bollinger, L., Ramillien, G., Rajaure, S., Sapkota, S., 2008. Seasonal variations of seismicity and geodetic strain in the Himalaya induced by surface hydrology. Earth Planet. Sci. Lett. 266, 332–344. https://doi.org/10.1016/j.epsl.2007.11.021.

Chen, X., Shearer, P., Abercrombie, R., 2012. Spatial migration of earthquakes within seismic clusters in Southern California: evidence for fluid diffusion. J. Geophys. Res., Solid Earth 117. https://doi.org/10.1029/2011JB008973.

Christiansen, L.B., Hurwitz, S., Ingebritsen, S.E., 2007. Annual modulation of seismicity along the San Andreas Fault near Parkfield, CA. Geophys. Res. Lett. 34. https://doi.org/10.1029/2006GL028634.

Cochran, E.S., Vidale, J.E., Tanaka, S., 2004. Earth tides can trigger shallow thrust fault earthquakes. Science 306, 1164–1166. https://doi.org/10.1126/science.1103961.

Craig, T.J., Chanard, K., Calais, E., 2017. Hydrologically-driven crustal stresses and seismicity in the New Madrid seismic zone. Nat. Commun. 8, 1–11. https://doi.org/10.1038/s41467-017-01696-w.

Fukuda, J., Johnson, K.M., 2021. Bayesian inversion for a stress-driven model of afterslip and viscoelastic relaxation: method and application to postseismic deformation following the 2011 MW 9.0 Tohoku-Oki earthquake. J. Geophys. Res., Solid Earth 126, e2020JB021620. https://doi.org/10.1029/2020JB021620.

Gao, S.S., Silver, P.G., Linde, A.T., Sacks, I.S., 2000. Annual modulation of triggered seismicity following the 1992 Landers earthquake in California. Nature 406, 500–504. https://doi.org/10.1038/35020045.

Gardner, J., Knopoff, L., 1974. Is the sequence of earthquakes in Southern California, with aftershocks removed Poissonian? Bull. Seismol. Soc. Am. 64, 1363–1367. https://doi.org/10.1785/BSSA0640051363.

Gauer, L.M., Chanard, K., Fleitout, L., 2023. Data-driven gap filling and spatio-temporal filtering of the grace and grace-fo records. J. Geophys. Res., Solid Earth 128, e2022JB025561. https://doi.org/10.1029/2022JB025561.

Harris, R.A., 1998. Introduction to special section: stress triggers, stress shadows, and implications for seismic hazard. J. Geophys. Res., Solid Earth 103, 24347–24358. https://doi.org/10.1029/98JB01576.

Hashimoto, C., Noda, A., Sagiya, T., Matsu'ura, M., 2009. Interplate seismogenic zones along the Kuril–Japan trench inferred from gps data inversion. Nat. Geosci. 2, 141–144. https://doi.org/10.1038/NGEO421.

Hayes, G.P., Moore, G.L., Portner, D.E., Hearne, M., Flamme, H., Furtney, M., Smoczyk, G.M., 2018. Slab2, a comprehensive subduction zone geometry model. Science 362, 58–61. https://doi.org/10.5066/F7PV6JNV.

Heki, K., 2003. Snow load and seasonal variation of earthquake occurrence in Japan. Earth Planet. Sci. Lett. 207, 159–164. https://doi.org/10.1016/S0012-821X(02)01148-2.

Heuret, A., Lallemand, S., Funiciello, F., Piromallo, C., Faccenna, C., 2011. Physical characteristics of subduction interface type seismogenic zones revisited. Geochem. Geophys. Geosyst. 12. https://doi.org/10.1029/2010GC003230.

Hirose, F., 2023. TidalStrain: tidal response tool. https://mri-2.mri-jma.go.jp/owncloud/s/tjqx7HfK8bD3KQf.

Hirose, F., Miyaoka, K., Hayashimoto, N., Yamazaki, T., Nakamura, M., 2011. Outline of the 2011 off the Pacific coast of Tohoku earthquake (Mw 9.0)—seismicity: foreshocks, mainshock, aftershocks, and induced activity. Earth Planets Space 63, 513–518. https://doi.org/10.5047/eps.2011.05.019.

Hirose, F., Maeda, K., Kamigaichi, O., 2019. Tidal forcing of interplate earthquakes along the Tonga-Kermadec Trench. J. Geophys. Res., Solid Earth 124, 10498–10521. https://doi.org/10.1029/2019JB018088.

Hsu, Y.J., Kao, H., Bürgmann, R., Lee, Y.T., Huang, H.H., Hsu, Y.F., Wu, Y.M., Zhuang, J., 2021. Synchronized and asynchronous modulation of seismicity by hydrological loading: a case study in Taiwan. Sci. Adv. 7, eabf7282. https://doi.org/10.1126/sciadv.abf7282.

International Seismological Centre, 2023. On-line bulletin. https://doi.org/10.31905/D808B830.

Johnson, C.W., Fu, Y., Bürgmann, R., 2017. Stress models of the annual hydrospheric, atmospheric, thermal, and tidal loading cycles on California faults: perturbation of background stress and changes in seismicity. J. Geophys. Res., Solid Earth 122, 10–605. https://doi.org/10.1002/2017JB014778.

Johnson, C.W., Fu, Y., Bürgmann, R., 2020. Hydrospheric modulation of stress and seismicity on shallow faults in southern Alaska. Earth Planet. Sci. Lett. 530, 115904. https://doi.org/10.1016/j.epsl.2019.115904.

Kano, M., Aso, N., Matsuzawa, T., Ide, S., Annoura, S., Arai, R., Baba, S., Bostock, M., Chao, K., Heki, K., et al., 2018. Development of a slow earthquake database. Seismol. Res. Lett. 89, 1566–1575. https://doi.org/10.1785/0220180021.

King, G.C., Stein, R.S., Lin, J., 1994. Static stress changes and the triggering of earthquakes. Bull. Seismol. Soc. Am. 84, 935–953. https://doi.org/10.1016/0148-9062(95)94484-2.

Lin, J., Stein, R.S., 2004. Stress triggering in thrust and subduction earthquakes and stress interaction between the southern San Andreas and nearby thrust and strike-slip faults. J. Geophys. Res., Solid Earth 109. https://doi.org/10.1029/2003JB002607.

Lordi, A.L., Neves, M., Custódio, S., Dumont, S., 2022. Seasonal modulation of oceanic seismicity in the Azores. Front. Earth Sci. 10. https://doi.org/10.3389/feart.2022.995401.

Lowry, A.R., 2006. Resonant slow fault slip in subduction zones forced by climatic load stress. Nature 442, 802–805. https://doi.org/10.1038/nature05055.

Lu, Z., Yi, H., Wen, L., 2018. Loading-induced Earth's stress change over time. J. Geophys. Res., Solid Earth 123, 4285–4306. https://doi.org/10.1029/2017JB015243.

Luttrell, K., Sandwell, D., 2010. Ocean loading effects on stress at near shore plate boundary fault systems. J. Geophys. Res., Solid Earth 115. https://doi.org/10.1029/2009JB006541.

Martens, H.R., 2016. Using Earth Deformation Caused by Surface Mass Loading to Constrain the Elastic Structure of the Crust and Mantle. Ph.D. thesis. California Institute of Technology.

Menemenlis, D., Campin, J.M., Heimbach, P., Hill, C., Lee, T., Nguyen, A., Schodlok, M., Zhang, H., 2008. Ecco2: high resolution global ocean and sea ice data synthesis. Mercator Ocean Q. Newsl. 31, 13–21.

Nishikawa, T., Matsuzawa, T., Ohta, K., Uchida, N., Nishimura, T., Ide, S., 2019. The slow earthquake spectrum in the Japan Trench illuminated by the S-net seafloor observatories. Science 365, 808–813. https://doi.org/10.1126/science.aax561.

Ozawa, S., Nishimura, T., Suito, H., Kobayashi, T., Tobita, M., Imakiire, T., 2011. Coseismic and postseismic slip of the 2011 magnitude-9 Tohoku-Oki earthquake. Nature 2011, 373–376. https://doi.org/10.1038/nature10227.

Ozawa, S., Nishimura, T., Munekane, H., Suito, H., Kobayashi, T., Tobita, M., Imakiire, T., 2012. Preceding, coseismic, and postseismic slips of the 2011 Tohoku earthquake, Japan. J. Geophys. Res., Solid Earth 117. https://doi.org/10.1029/2011JB009120.

Reasenberg, P., 1985. Second-order moment of central California seismicity, 1969–1982. J. Geophys. Res., Solid Earth 90, 5479–5495. https://doi.org/10.1029/JB090iB07p05479.

Rodell, M., Houser, P., Jambor, U., Gottschalck, J., Mitchell, K., Meng, C.J., Arsenault, K., Cosgrove, B., Radakovich, J., Bosilovich, M., et al., 2004. The global land data assimilation system. Bull. Am. Meteorol. Soc. 85, 381–394. https://doi.org/10.1175/BAMS-85-3-381.

Rodell, M., Velicogna, I., Famiglietti, J.S., 2009. Satellite-based estimates of groundwater depletion in India. Nature 460, 999–1002. https://doi.org/10.1038/nature08238.

Rubinstein, J.L., La Rocca, M., Vidale, J.E., Creager, K.C., Wech, A.G., 2008. Tidal modulation of nonvolcanic tremor. Science 319, 186–189. https://doi.org/10.1126/science.1150558.

Scanlon, B.R., Zhang, Z., Save, H., Sun, A.Y., Schmied, H.M., van Beek, L.P.H., Wiese, D.N., Wada, Y., Long, D., Reedy, R.C., Longuevergne, L., Döll, P., Bierkens, M.F.P., 2018. Global models underestimate large decadal declining and rising water storage trends relative to grace satellite data. Proc. Natl. Acad. Sci. 115, E1080–E1089. https://doi.org/10.1073/pnas.1704665115. arXiv: https://www.pnas.org/doi/pdf/10.1073/pnas.1704665115.

Schober, P., Boer, C., Schwarte, L.A., 2018. Correlation coefficients: appropriate use and interpretation. Anesth. Analg. 126, 1763–1768. https://doi.org/10.1213/ANE.0000000000002864.

Scholz, C.H., Tan, Y.J., Albino, F., 2019. The mechanism of tidal triggering of earthquakes at mid-ocean ridges. Nat. Commun. 10, 1–7. https://doi.org/10.1038/s41467-019-10605-2.

Steer, P., Simoes, M., Cattin, R., Shyu, J.B.H., 2014. Erosion influences the seismicity of active thrust faults. Nat. Commun. 5, 1–7. https://doi.org/10.1038/ncomms6564.

Steer, P., Jeandet, L., Cubas, N., Marc, O., Meunier, P., Simoes, M., Cattin, R., Shyu, J.B.H., Mouyen, M., Liang, W.T., Theunissen, T., Chiang, S.H., Hovius, N., 2020. Earthquake statistics changed by typhoon-driven erosion. Sci. Rep. 10, 10899. https://doi.org/10.1038/s41598-020-67865-y.

Stein, R.S., 1999. The role of stress transfer in earthquake occurrence. Nature 402, 605–609. https://doi.org/10.1038/45144.

Tamaribuchi, K., 2018. Evaluation of automatic hypocenter determination in the JMA unified catalog. Earth Planets Space 70, 1–10. https://doi.org/10.1186/S40623-018-0915-4.

Tanaka, S., Ohtake, M., Sato, H., 2004. Tidal triggering of earthquakes in Japan related to the regional tectonic stress. Earth Planets Space 56, 511–515. https://doi.org/10.1186/BF03352510.

Tanaka, Y., Sakaue, H., Kano, M., Yabe, S., 2023. A combination of tides and nontidal variations in ocean bottom pressure may generate interannual slip fluctuations in the transition zone along a subduction plate interface. Geod. Geodyn. 14, 43–51. https://doi.org/10.1016/j.geog.2022.09.001.

Tapley, B.D., Bettadpur, S., Watkins, M., Reigber, C., 2004. The gravity recovery and climate experiment: mission overview and early results. Geophys. Res. Lett. 31. https://doi.org/10.1029/2004GL019920.

Toda, S., Stein, R.S., Beroza, G.C., Marsan, D., 2012. Aftershocks halted by static stress shadows. Nat. Geosci. 5, 410–413. https://doi.org/10.1038/NGEO1465.

Tsuruoka, H., Ohtake, M., Sato, H., 1995. Statistical test of the tidal triggering of earthquakes: contribution of the ocean tide loading effect. Geophys. J. Int. 122, 183–194. https://doi.org/10.1111/j.1365-246X.1995.tb03546.x.

Uchida, N., Iinuma, T., Nadeau, R.M., Bürgmann, R., Hino, R., 2016. Periodic slow slip triggers megathrust zone earthquakes in northeastern Japan. Science 351, 488–492. https://doi.org/10.1126/science.aad3108.

Ueda, T., Kato, A., 2019. Seasonal variations in crustal seismicity in San-in district southwest Japan. Geophys. Res. Lett. 46, 3172–3179. https://doi.org/10.1029/2018GL081789.

Ueda, T., Kato, A., Johnson, C.W., Terakawa, T., 2024. Seasonal modulation of crustal seismicity in northeastern Japan driven by snow load. J. Geophys. Res., Solid Earth 129, e2023JB028217. https://doi.org/10.1029/2023JB028217.

Uhrhammer, R., 1986. Characteristics of northern and central California seismicity. Earthq. Notes 57, 21. https://doi.org/10.1130/dnag-csms-neo.99.

Wang, L., Shum, C.K., Simons, F.J., Tapley, B., Dai, C., 2012. Coseismic and postseismic deformation of the 2011 Tohoku-Oki earthquake constrained by GRACE gravimetry. Geophys. Res. Lett. 39, 7301. https://doi.org/10.1029/2012GL051104.

Wang, X., de Linage, C., Famiglietti, J., Zender, C.S., 2011. Gravity recovery and climate experiment (grace) detection of water storage changes in the three gorges reservoir of China and comparison with in situ measurements. Water Resour. Res. 47. https://doi.org/10.1029/2011WR010534.

Warren, L.M., Baluyut, E.C., Osburg, T., Lisac, K., Kokkinen, S., 2015. Fault plane orientations of intermediate-depth and deep-focus earthquakes in the Japan-Kuril-Kamchatka subduction zone. J. Geophys. Res., Solid Earth 120, 8366–8382. https://doi.org/10.1002/2015JB012463.

Wiemer, S., 2001. A software package to analyze seismicity: ZMAP. Seismol. Res. Lett. 72, 373–382. https://doi.org/10.1785/gssrl.72.3.373.

Woessner, J., Wiemer, S., 2005. Assessing the quality of earthquake catalogues: estimating the magnitude of completeness and its uncertainty. Bull. Seismol. Soc. Am. 95, 684–698. https://doi.org/10.1785/0120040007.

Xue, L., Fu, Y., Johnson, C.W., Otero Torres, J.J., Shum, C., Bürgmann, R., 2021. Seasonal seismicity in the Lake Biwa region of central Japan moderately modulated by lake water storage changes. J. Geophys. Res., Solid Earth 126, e2021JB023301. https://doi.org/10.1029/2021JB023301.

Yan, R., Chen, X., Sun, H., Xu, J., Zhou, J., 2023. A review of tidal triggering of global earthquakes. Geod. Geodyn. 14, 35–42. https://doi.org/10.1016/j.geog.2022.06.005.

Zaliapin, I., Ben-Zion, Y., 2013. Earthquake clusters in southern California I: identification and stability. J. Geophys. Res., Solid Earth 118, 2847–2864. https://doi.org/10.1002/jgrb.50179.